Contents lists available at ScienceDirect

Applied Materials Today

Deposition of high-quality, nanoscale SiO$_2$ films and 3D structures

Paul Cannon [a,*], Enda McGlynn [a,b,*], Darragh O'Neill [a,b], Conor Darcy [a], Erin Rouse [a], Robert O'Connor [a,b], Brian Freeland [c], Barry O'Connell [d], Jennifer Gaughran [a]

[a] School of Physical Sciences, Dublin City University, Dublin, Ireland
[b] National Centre for Plasma Science & Technology, Dublin City University, Dublin, Ireland
[c] School of Biotechnology, Dublin City University, Dublin, Ireland
[d] Nano Research Facility (NRF), Dublin City University, Dublin, Ireland

ARTICLE INFO

ABSTRACT

Silicon dioxide (SiO$_2$) is ubiquitous in biomedical diagnostics and other applications as a capture medium for nucleic acids and proteins. Diagnostic devices have seen rapid miniaturisation in recent years, due to the increased demand for portable point-of-care diagnostics. However, there are increasing challenges with incorporating SiO$_2$ nanostructures into diagnostic devices, due to the complexity of nanostructured SiO$_2$ synthesis, often involving etching and chemical vapour deposition under high vacuum conditions.

We report a novel and straightforward method for deposition of high-quality, nanoscale SiO$_2$ films and 3D SiO$_2$ structures using thermal decomposition of polydimethylsiloxane (PDMS), in a furnace at atmospheric pressure at 500 °C. This method allows individual nanometre controllability of conformal pinhole-free layers on a variety of materials and morphologies. The temperature ramp rate is a key factor in determining the SiO$_2$ deposit morphology, with slower ramp rates leading to highly conformal 2D films and faster ones yielding 3D nanodentrite structures. For the 2D films, the film thickness, as determined by spectroscopic ellipsometry and confirmed by SEM data, is shown to correlate excellently with initial PDMS source material mass in the thickness range 0.8–18 nm. Fits to ellipsometry models confirm that the refractive index of the deposited film matches the expected value for SiO$_2$, while electrical breakdown measurements confirm that the breakdown strength of the films is comparable to that of high-quality thermal oxides. Depositions on high aspect ratio ZnO nanostructures are shown to be highly conformal, leading to core-shell ZnO-SiO$_2$ nanostructures whose shell thickness is in excellent agreement with the expected values from deposition on planar substrates. At faster ramp rates an abrupt morphological transition is seen to a deposit which displays a 3D nanodentrite morphology. The possibilities for applications of both morphologies (and core-shell combinations with other nanostructured materials) in biosensing and related areas are briefly discussed, and the DNA capture capabilities of each nanostructure are measured. The high aspect ratio nanodendrite structures allow for significant DNA capture within microfluidic devices in the presence of low DNA concentrations, with a maximum average capture efficiency of 43.4 % achieved in the presence of 10 ng/mL of DNA, which is an improvement by a factor of ∼ 3 over planar Si surfaces. Improvements by factors of >10 over planar surfaces were achieved at higher DNA concentrations of 100 and 1000 ng/mL.

1. Introduction

1.1. SiO$_2$ importance in biomedical and related applications

Silicon dioxide (SiO$_2$) is one of the most widely utilised materials in biomedical and related applications, due to its relative biocompatibility and affinity for DNA and protein interactions compared to other commonly used materials like gold and silver. However, incorporating SiO$_2$ materials and structures into portable, lab-on-a-chip (LoC) based technologies has proved challenging [1]. Traditionally, lab based nucleic acid detection is performed using SiO$_2$ microbeads, however, incorporating these microbeads into microfluidic channels produces inconsistent and irreproducible results [1,2]. Recently, there has been a shift towards the use of Si and SiO$_2$ micropillars in microfluidic LoC and

biosensing devices to overcome these challenges [3–6]. These micropillars are not only useful for DNA analysis, but a variety of other applications in areas like cell biology [7], targeted drug delivery [8], and photovoltaics [9] etc.

1.2. Challenges in the fabrication of nanostructured SiO_2 and potential for synergistic leveraging of properties of other materials

It is clear that micro- or nanostructuring of the SiO_2 will increase the surface area per unit volume of material and this is a particularly promising route for exploration in this area of materials science [10,11]. However the creation of SiO_2 nanostructured deposits is quite challenging, due to the complexity of SiO_2 deposition and structuring methods, often involving etching and chemical vapour deposition (CVD) under high vacuum condition [3].

By contrast, other metal oxide materials, notably ZnO, readily form a variety of high surface to volume ratio nanostructured morphologies using both chemical bath and physical vapour deposition methods, in a self-assembled bottom-up manner. However, the surface properties of ZnO differ significantly from SiO_2, and hence their interaction with biological species such as nucleic acids and proteins is quite different to that of SiO_2 [12–15].

The ability to create nanostructured SiO_2 deposits using relatively simple laboratory-based methods is thus an important research challenge, whose successful attainment should enable significant advances in research areas such as biosensors and biomedical devices.

1.3. Novel method for realisation of nanoscale SiO_2 deposits to overcome these challenges

We report here a novel and straightforward method for deposition of high-quality, nanoscale SiO_2 films and 3D SiO_2 structures using thermal decomposition of polydimethylsiloxane (PDMS), in a furnace in atmospheric pressure at 500 °C. When used for 2D films, this method allows individual nanometre controllability of conformal pinhole-free layers on a variety of materials. This can then be used in conjunction with other bottom-up nanostructured oxides such as ZnO, which allows the creation of high surface to volume ratio core-shell nanostructures with SiO_2 outer shells whose surface properties are well suited to interactions with biological species, and are well understood and indeed can be further tailored and customised using surface treatments such as plasma exposure. The ability to grow SiO_2 shell layers of thicknesses < 10 nm conformally is extremely important because it means that the original morphology and surface to volume ratio of the core nanostructures will be faithfully preserved, whereas a much thicker shell layer could blanket the original core nanostructures completely. Furthermore the core-shell structure using conductive oxide cores such as ZnO may enable additional device functionality and selectivity by the use of voltages applied to the network of core nanostructures. The nanostructured morhology will also lead to significant field enhancement effects which would increase interactions with charged species in solution.

When used for 3D nanostructures this deposition method yields a deposit with a bottom-up 3D nanodentrite structure with an intrinsically high surface to volume ratio.

2. Methods

2.1. ZnO scaffold synthesis

ZnO nanorods (NRs) were synthesised using both chemical bath deposition (CBD) and physical vapour deposition (PVD) technicques. The ZnO scaffolds were grown using a three-step process; firstly chemical solution seeding, followed by CBD, and finally carbothermal reduction vapour phase transport growth (CTRVPT). 5 mM of zinc acetate dihydrate in anhydrous ethanol was used for the seeding. 4 $\mu L/cm^2$ of this solution was drop coated onto a clean silicon wafer substrate and

allowed to evaporate for 20 seconds before being rinsed with fresh anhydrous ethanol and dried immediately with a nitrogen stream. This was repeated for a total of 5 dropcoats. The substrates were then annealed for 20 minutes at 350 °C to create ZnO seed layers. Seeded substrates were then submerged in 40 mL of a 25 mM solution of zinc acetate dihydrate in deionised water at 65 °C. The substrates were removed from the bath after 90 minutes and rinsed with deionised water and left to dry in air. This results in the growth of sufficiently dense array of ZnO NRs that can be considered a compact ZnO film which we call the buffer layer. It is from this buffer layer that CTRVPT NRs were grown. 60 mg of both ZnO and graphite powders were carefully mixed via mortar and pestle to a create a homogenous powder which was spread across a 2 cm length of an alumina crucible. Substrates coated in the ZnO buffer layer were suspended directly above the ZnO/graphite mixture and the alumina boat containing sample and powder was loaded into a single temperature zone horizontal tube furnace (Lenton Thermal Designs). The boat was heated to 925°C under a 90 sccm argon flow and this temperature was maintained for 40 minutes. Further details may be found in previous reports from our group [16,17].

2.2. SiO_2 Coating

Planar substrates (both Si wafer coupons and ZnO thin films), as well as ZnO nanostructured deposits were coated in SiO_2 using a novel PVD technique developed by our group, which is based on the thermal decomposition of polydimethlysiloxane (PDMS) in air. The technique is similar to that reported in our previous work, but with some slight differences which enable nanometre-scale control of film thickness, and also deposit morphology [18]. To briefly summarise, varying masses of PDMS were placed at one end of an alumina crucible, with the substrates positioned at the opposite end, 5.5 cm away from the block of PDMS, lying across the boat in the manner shown in Fig. 1. This alumina boat was positioned inside a hollow quartz tube (3.8 cm inner diameter), and the quartz tube was placed in the centre of a muffle furnace (Nabertherm Muffle Furnace LT 3/11/B410), with the samples to be coated located between the PDMS block and the furnace exhaust. For the case of substrates $\leq$ 1 cm^2, which were too narrow to be suspended across the alumina crucible, we placed substrates on top of a larger Si wafer piece which was suspended across the crucible. The furnace was heated to 500 °C using ramp rates from 1 °C/min up to 40 °C/min, and this temperature was maintained for two hours. The amount of deposit is controlled by the PDMS mass. The temperature ramp rate allowed us to control the deposit morphology, with slower ramp rates leading to highly conformal 2D films with an abrupt transition at a heating rate of > 2 °C/min to deposits with 3D nanodentritic morphologies.

The experimental configuration is largely similar to that reported in our previous work [18]. In that previous work small pieces of Si were used to mark portions of the substrate during growth to enable subsequent profilometry measurements of SiO_2 deposit thickness. Using this method we determined using contact profilometry that 6 mg of PDMS, heated to 500 °C at a rate of 1 °C/min provides an SiO_2 thickness of 25-50 nm. Since that work we have altered our standard characterisation protocols to use spectroscopic ellipsometry (SE) to routinely measure deposit thicknesses, with occasional use of FESEM to confirm the SE measurements. The removal of the masking Si pieces has had a significant effect on the vapour flow close to the substrate and had led to a significantly reduced deposition rate, allowing much thinner films to be deposited with thicknesses as low as 0.8 nm, as shown below.

The properties of the 2D films were compared to those of a thermal SiO_2 film of the same thickness, supplied by an industrial partner.

2.3. Characterisation

The SiO_2 deposited using this approach was characterised using x-ray photoelectron spectroscopy (XPS) using a Scienta Omicron x-ray photoelectron spectrometer with a monochromated Al Kα source
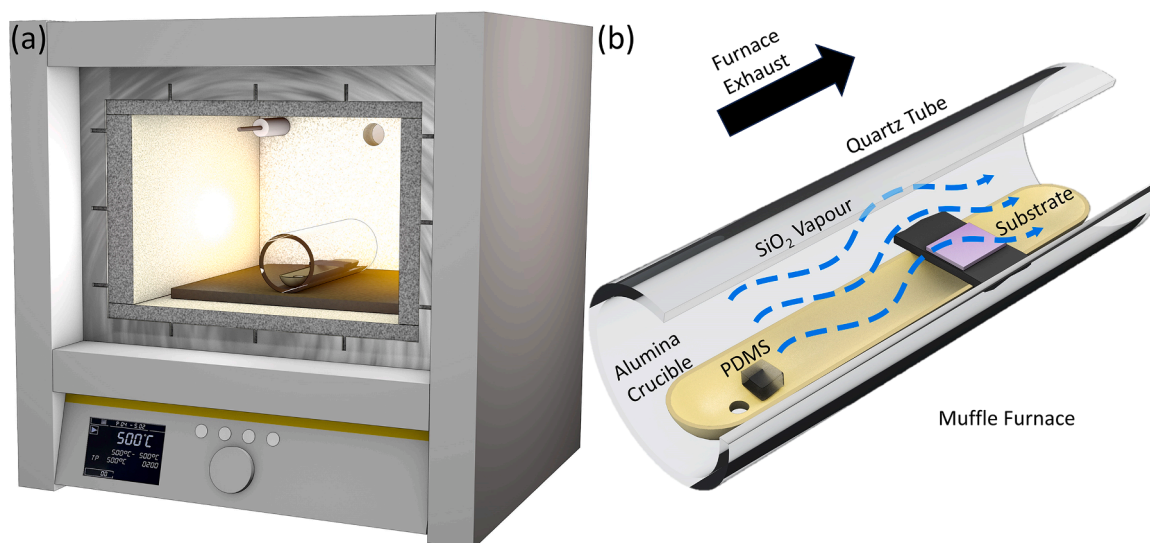
Fig. 1. (a) Schematic diagram of PDMS-based SiO$_2$ deposition. (b) Labelled components of PDMS-based SiO$_2$ deposition.

(1486.7 eV), as well as by scanning electron micropscopy (SEM) using a thermionic emission Karl-Zeiss EVO LS15 scanning electron system, with a LaB$_6$ filament and a Hitachi S5500 Field Emission SEM (FESEM) with energy-dispersive x-ray spectroscopy (EDX) capabilities. The film thicknesses and refractive indices were characterised by SE using a J.A. Woollam M-2000UI spectroscopic ellipsometer. SE data was analysed using the Woollam CompleteEASE software, and was fit with the Oxide on Si model (i.e. a planar SiO$_2$ film on Si with native oxide) to extract thickness values. Atomic force microscopy (AFM) data were acquired using a Bruker ICON AFM system in PeakForce Tapping ScanAsyst mode. AFM measurements were performed with a scan rate of 0.5 Hz and with 512 samples per line.

Electrical breakdown characterisation of the SiO$_2$ films was performed in an in-house system based on a Keithley 4200 semiconductor characterisation system, with voltages up to 21 V applied to the samples via a probe station. A 12×12 array of rectangular Au contact pads (area $(4.8 \pm 0.8) \times 10^{-3}$ mm^2) were deposited using an Edwards AUTO 306 vacuum coater. An Au wire was evaporated using a tungsten filament operated under a $\sim$ 2.5-3.0 kV voltage and $\sim$ 20 mA current. The data were analysed using a 2-parameter Weibull distribution [19,20].

2.3. DNA Capture

The DNA capture capabilities of each nanostructure morphology were investigated under flow within a microfluidic chip, and schematic diagrams of the chip design can be seen in the electronic supporting information (ESI; fig. S.1) alongside a description of the fabrication and assembly procedure. DNA solutions were made of calf thymus DNA dissolved in a binding buffer solution (20:1 ratio of deionised water and Qiagen PB buffer). The microfluidic channels were 14×3×0.086 mm in size (l x w x h) and 1 mL of DNA solutions of various concentrations (10, 100, and 1000 ng/mL) was flowed over the nanostructures at a rate of 30 µL/min and then into a beaker for collection. Fluorescence spectroscopy of the DNA solutions before (DNA$_i$) and after (DNA$_f$) flowing through the microfluidic chips allows us to calculate the amount of DNA captured (DNA$_c$) by the nanostructures by the following equation:

$$DNA_C = DNA_i - DNA_f \tag{1}$$

DNA concentrations were measured using the Quant-iT PicoGreen dsDNA Assay kit. The assays were performed in a 96-well plate, where a 1:1 aliquot of sample and dye (100 µL each) was placed in each well, with the binding buffer serving as the background. The plate was covered in reflective foil, and the samples and dye were left to incubate

for 5 min before being placed in a Tecan Infinite Pro 200 M Plex spectrofluorometer for measurement. The excitation (λ_{ex}) and emission (λ_{em}) wavelengths were 480 nm and 520 nm, respectively.

3. Results and Discussion

3.1. Effects of temperature ramp rates on deposit morphology

We have examined the effect of changes in the ramp rate of the furnace from 1 °C/min up to 40 °C/min in our new growth configuration, since previous work has established that the temperature ramp rate is a significant parameter in the decomposition of PDMS. Since the products of the thermal decomposition of PDMS depend on the temperature ramp rate, this affects the degree of depolymerisation [18,21, 22]. SEM data for these studies is shown in Fig. 2 below, in both plan view and cross-sectional view.

At the lowest heating rates (1 °C/min) flat thin film deposits are seen for PDMS masses up to $\sim$ 65 mg, which will be studied in more detail in Section 3.2 below. We note that evidence of very small 3D dendritic structures is seen when using large PDMS masses ($\geq$ 70 mg) even at the lowest heating rates.

At a heating rate of $\sim$ 2–3 °C/min however a sharp change in the deposit morphology is seen, whereby the deposited material no longer forms a thin planar film but rather a nanoscale 3D dendritic structure. We have explored heating rates up to 40 °C/min and the dendritic morphology is observed up to the maximum heating rate obtainable in our furnace (40 °C/min). Previous studies of the thermal degradation mechanisms of PDMS report that PDMS will form ceramic silicon oxycarbide at high heating rates [21]. However, EDX analysis of the SiO$_2$ structures shown in Fig. 2 and the ESI (Fig. S.2) confirms pure SiO$_2$ stoichometry, with 20 and 40 °C/min dendritic structures having Si:O ratios of 1:2.1 and 1:1.9 respectively.

The SEM data are supported by our SE measurements and fits to the Oxide on Si model, as shown in Fig. 3 below. The SE data for the samples grown with a heating rate of 1 °C/min all fit the model very well, with an MSE of < 10. By contrast, attempts to fit the samples with the 3D dendritic structures with the same model yielded extremely poor fits (MSE of > 100), as expected given the model used.

The deposition configuration resembles that of glancing/oblique angle deposition (GLAD) techniques which produce characteristic porous nanostructures at precise deposition angles [23]. However, these techniques are often performed by magnetron sputtering under vacuum, and it is the high kinetic energy vapour species that do not undergo any
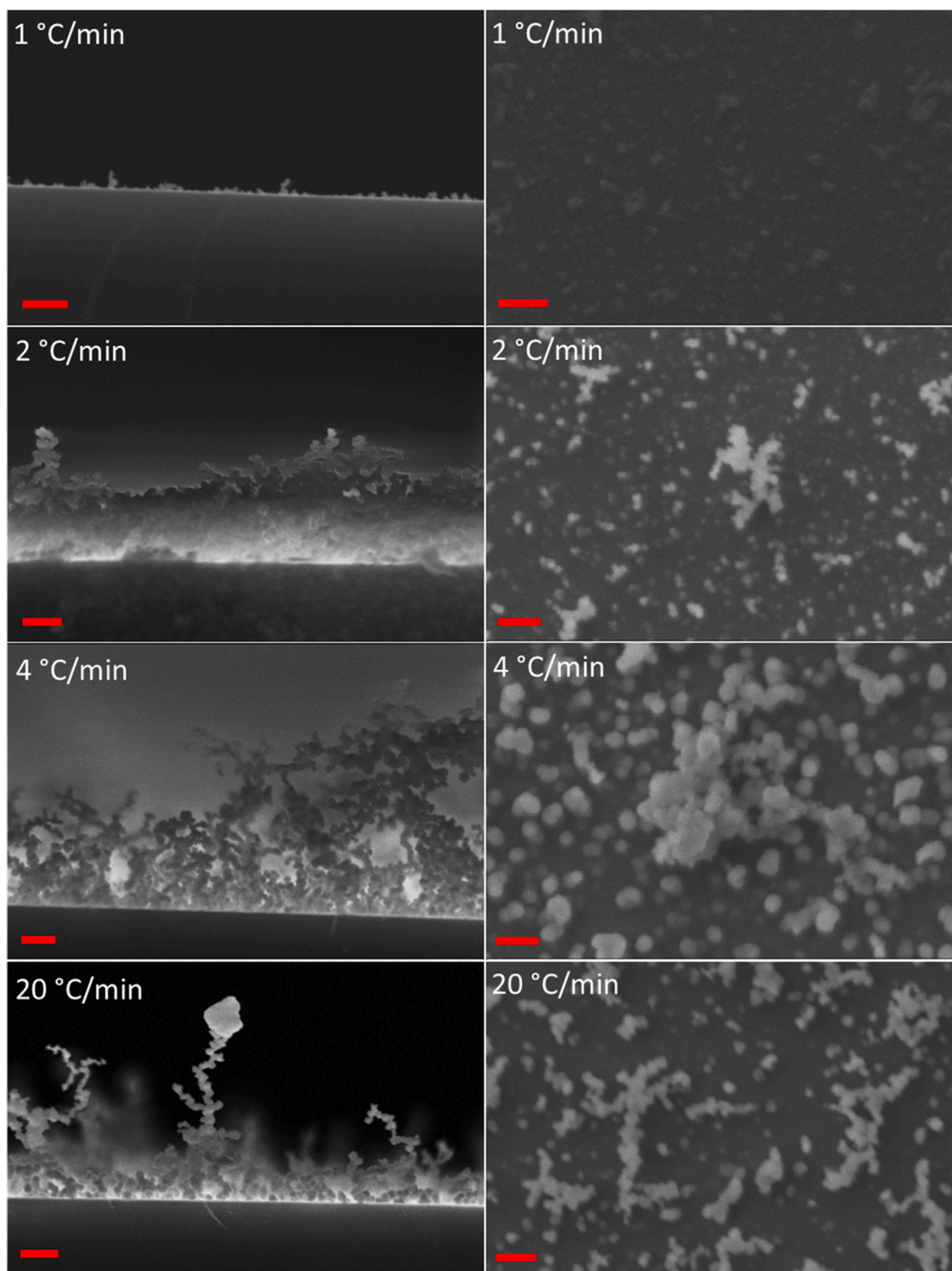
Fig. 2. SEM data showing effects of heating rate on SiO$_2$ deposition morphology using a constant PDMS mass of 70 mg. Cross-sectional images are shown on the left and the corresponding plan-view image is shown on the right. The scale bar in all images represents 1 μm.

collisions between source and substrate that give rise to well-defined, tilted nanostructure arrays [24]. The deposition reported in our work is rather different since it is performed by evaporation in air at atmospheric pressure, giving rise to low kinetic energy vapour species. Nonetheless we believe that the large interspacing of the 3D dendritic structures in Fig. 2 very probably arises from the shadowing effects which are commonly seen in GLAD processes [25].

As noted in Section 1.2, the creation of SiO$_2$ nanostructured deposits is quite challenging and thus this morphological transition is an interesting feature since it offers an effective route for the direct bottom-up creation of nanostructured SiO$_2$ in a straightforward manner.

3.2. Studies of SiO$_2$ thin films deposited using slow heating rates

As noted in Section 3.1, the SiO$_2$ films deposited at the lower heating rates show a thin film morphology, with the film thicknesses linearly dependent on the mass of PDMS used. Fig. 3 shows a regression plot of the thickness of the SiO$_2$ films deposited at a heating rate of 1 °C/min versus the mass of PDMS source material used. There is an excellent correlation, and one can see that ultra-thin SiO$_2$ films with thicknesses down to ~ 1 nm can be reliably and reproducibly grown using this method. The results in Fig. 3 demonstrate a high degree of thickness controllability at an individual nanometre scale. Large increases in
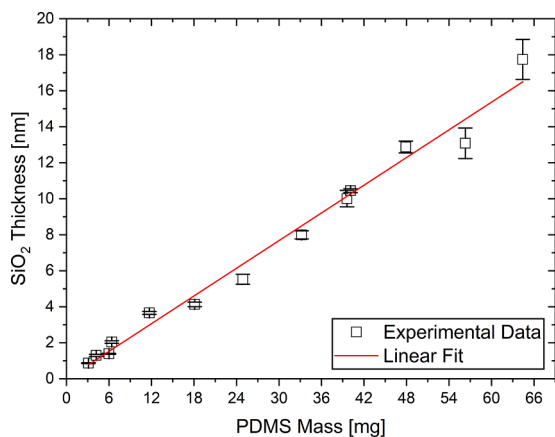
Fig. 3. Thickness vs PDMS source mass determined via SE. The slope is 0.256 ± 0.010 nm/mg, and the intercept is -0.015 ± 0.335 nm, with an r^2 value of 0.984. The error bars represent the standard deviation from five independent measurements of each sample.

source mass are required to increase the SiO_2 deposition by sub-nanometre thicknesses. This deposition process demonstrates excellent controllability, despite the fact that it is performed at atmospheric pressure using a relatively simple experimental geometry.

AFM data of these SiO_2 thin films are shown in Fig. 4, as well as data from a thermal oxide provided by an industrial partner. The data for PDMS-based depositions are quite featureless, speaking to the flat, thin

film morphology, which is confirmed by the cross-sectional FESEM data of the Au/SiO_2 structure shown in Fig. 5 (the residual roughness in these images being due to the granularity of the Au layers).

The growth technique leads to successful deposition on both Si and ZnO materials, with similar deposited thicknesses when using the same PDMS source material mass.

The coatings also display excellent conformality, which is shown by the FESEM and EDX data in Figs. 5 and 6. The data in Fig. 5 show the confirmality of the coating on uneven Au films with various SiO_2 thicknesses, while the data in Fig. 6 show the conformality of coating on physical vapour deposited ZnO NR cores with a nominal 10.5 nm SiO_2 shell deposition.

The data in Fig. 6 show an excellent conformal coating morphology at the single NR level on structures which are very different to planar substrates, as the regression line in Fig. 3 predicts a SiO_2 thickness of 11.2 nm. Further STEM, SEM and EDX data on similar structures are shown in the ESI (Figs. S.3 and S.4). The average nominal shell thickness (11.2 nm), determined from the mass of PDMS source material (43.6 mg) using the regression line in Fig. 3 is in excellent agreement with the measured shell thicknesses on individual NRs determined using the EDX data from the FESEM system (10.5 ± 3.0 nm). This again indicates that the deposition technique is not strongly dependent on the substrate material.

The conformality, and full coverage (i.e. absence of pinholes), of the thin films was studied using both AFM (as shown in Fig. 4) and XPS. We used XPS to investigate SiO_2 coatings deposited on flat ZnO buffer layers (under similar conditions to those deposited on Si substrates), the latter to provide elemental discrimination between film and substrate.
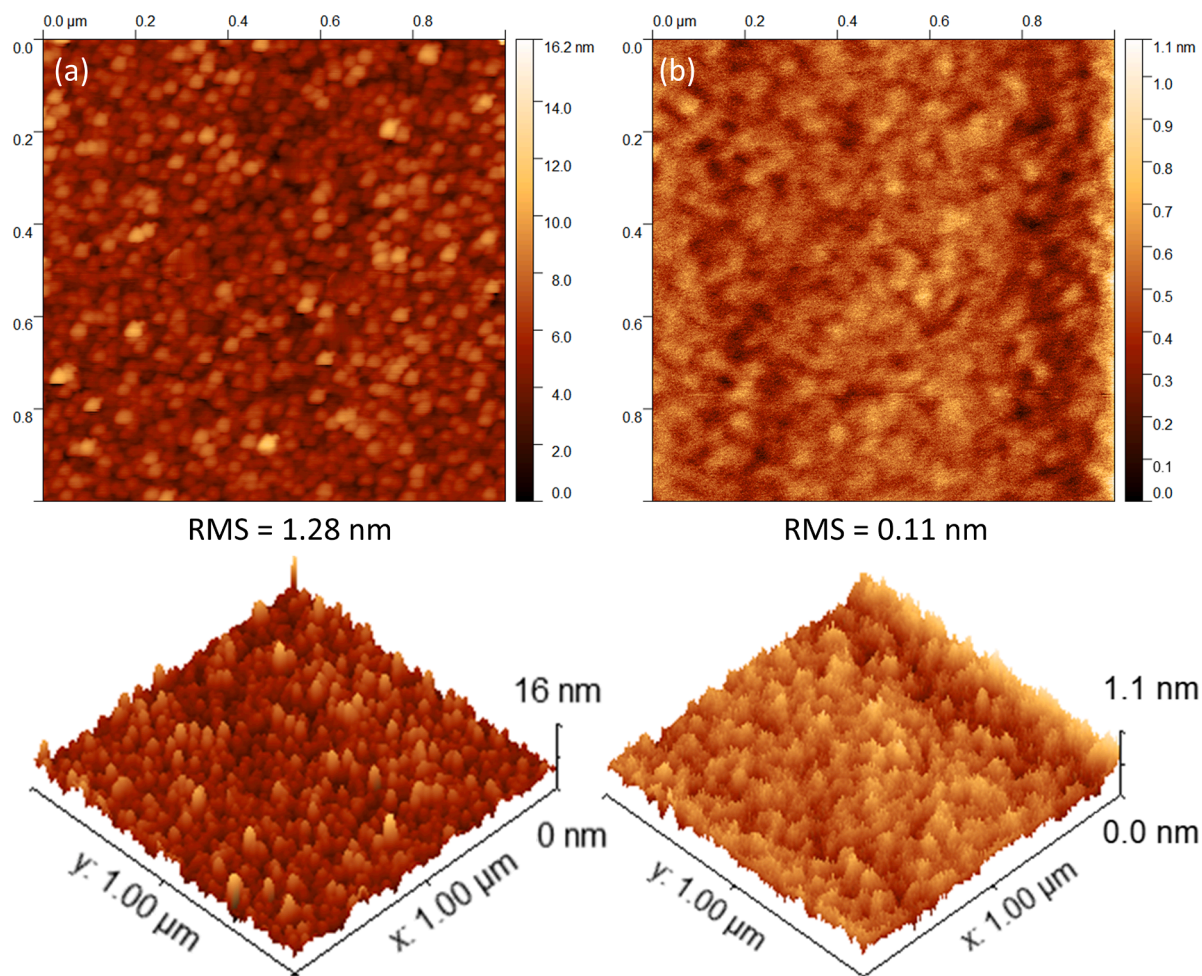

Fig. 4. AFM data of nominal 11.5 nm SiO_2 films. (a) PDMS-Based SiO_2 and (b) industrial thermal oxide.
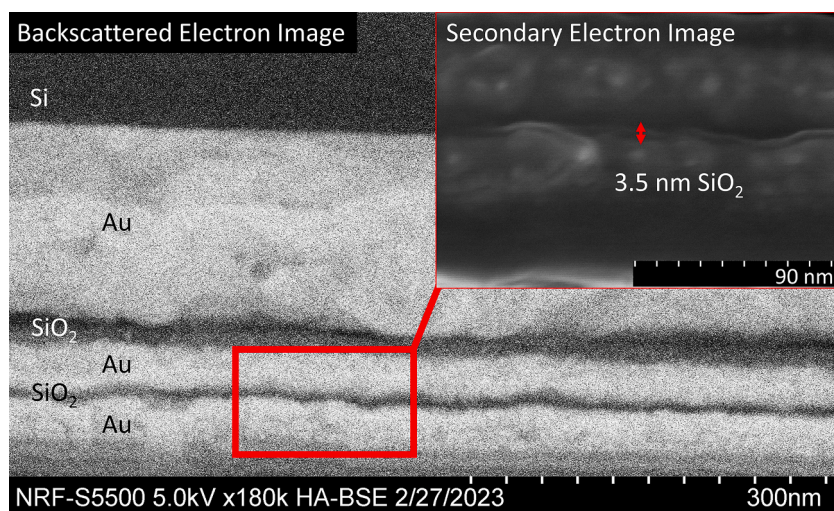
Fig. 5. Cross-sectional FESEM data of planar SiO$_2$ films. PDMS-based SiO$_2$ films (dark regions) were deposited between e-beam evaporated Au layers (bright regions) to obtain sufficient contrast for imaging. The substrate is at the top of the image.
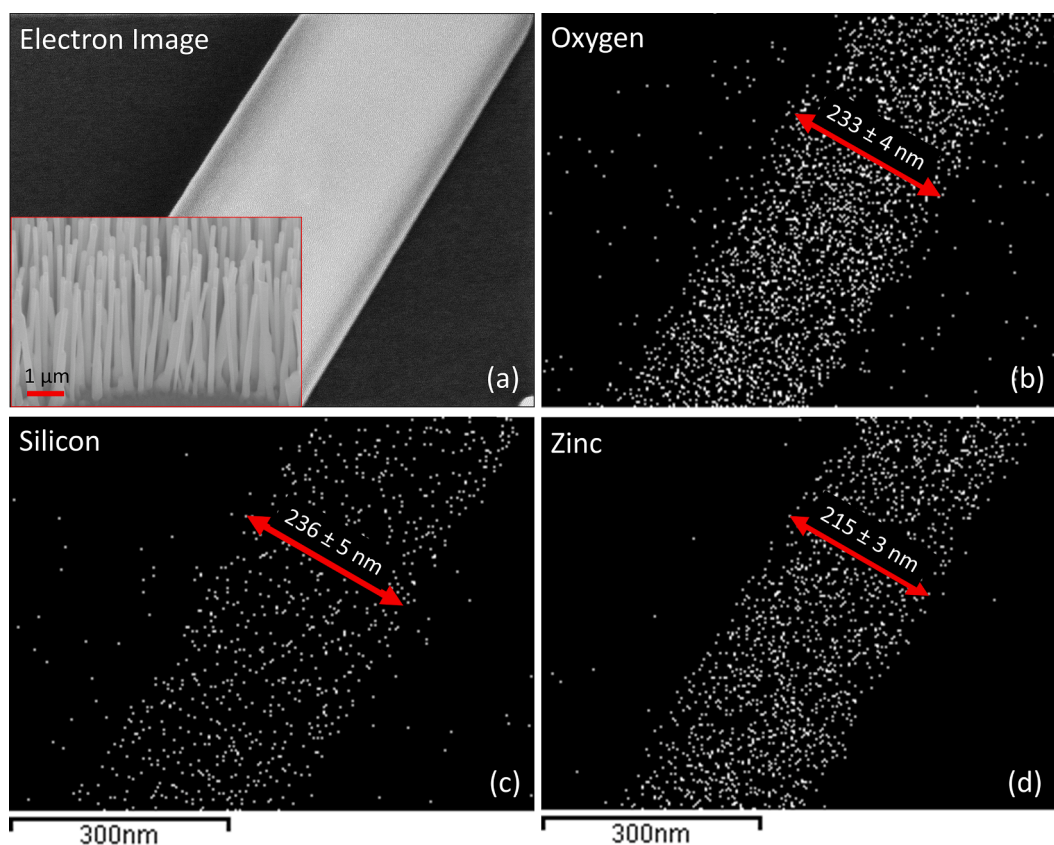

Fig. 6. (a) FESEM image of a core-shell ZnO-SiO$_2$ NR with an aspect ratio of 20 (Inset: Lower magnification SEM image of vertically aligned CTRVPT ZnO NR array tilted by 30°). (b), (c), and (d) corresponding EDX images of the characteristic O, Si, and Zn x-ray emission from (a).

The Zn 2p signal was specifically studied to determine coverage of the two coating methods. The electron inelastic mean free path of ∼ 1–2 nm means that for uniform and full coverage films the Zn 2p signal should be virtually undetectable for thicknesses ≥ 10 nm given our Al Kα x-ray source [26–28]. The XPS results for depositions on planar substrates can be seen below in Fig. 7.

The XPS results show the full coverage and conformality of our PDMS based deposition. The PDMS deposition shows clear supression of both Zn peaks located at 1022 and 1045 eV with coating thicknesses of ∼ 10

nm, which is at the limit of XPS sensitivity for electrons with a kinetic energy of <500 eV. In a conformal, uniform, dense and pinhole-free coating, the concentration of photoelectrons emanating from an underlying layer of this thickness will be beyond the detection limits of conventional XPS, which is what we see in the samples coated with PDMS deposited SiO$_2$. This effect is further illustrated by the O 1s spectra which shows two peaks, with the lower energy peak (531.5 eV) indicating the metal oxide bonding of ZnO, and the higher energy peak (533.5 eV) being that of the insulating SiO$_2$. With increasing PDMS
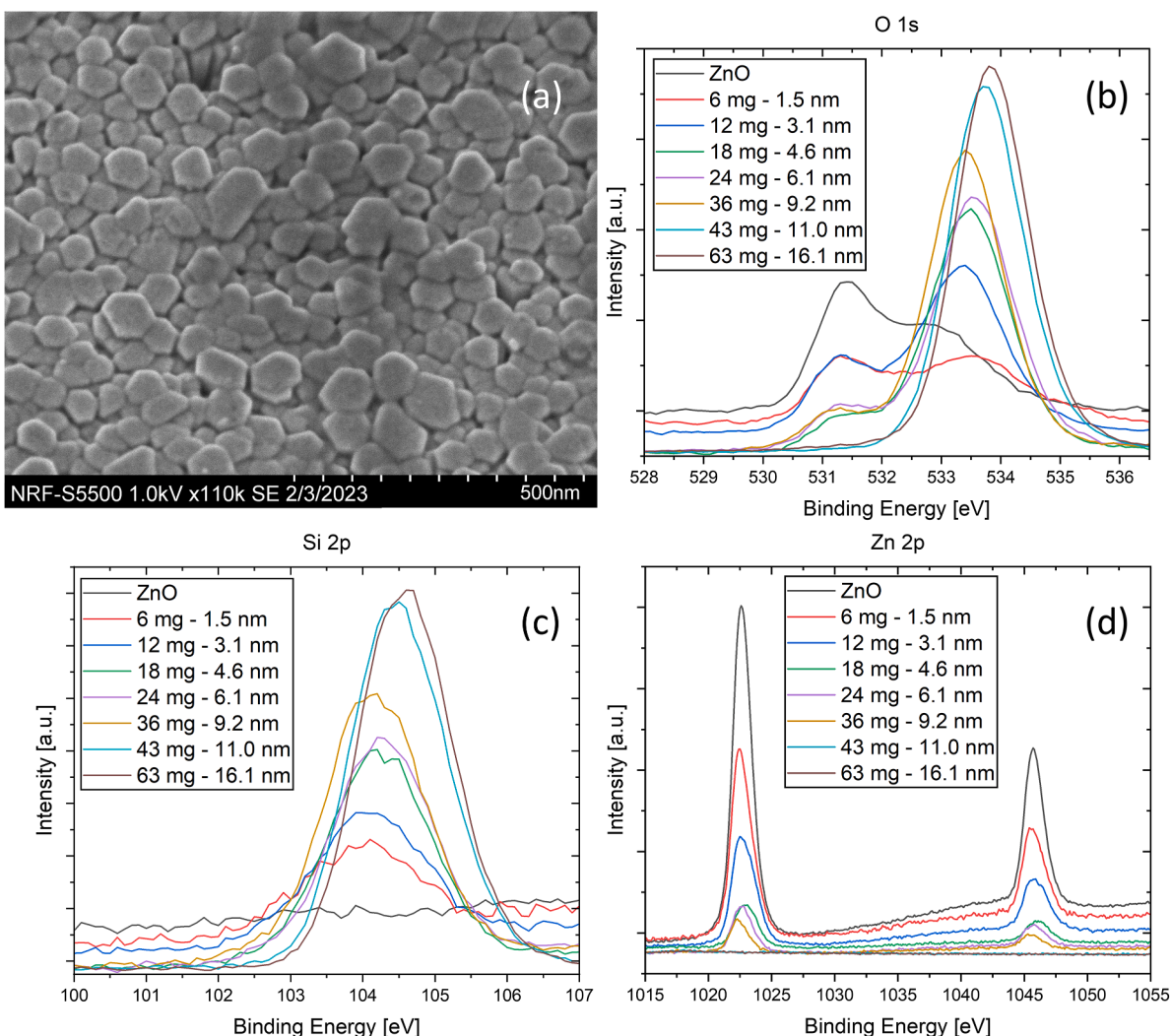
Fig. 7. (a) FESEM image of compact CBD ZnO planar NR films used to study SiO$_2$ deposition on non-Si substrates. (b) XPS spectra of the O 1s orbital region of sample (a) coated using varying amounts of PDMS. (c) XPS spectra of the Si 2p orbital region (d) XPS spectra of the Zn 2p orbital region.

mass, we see a decrease in the 531.5 eV peak intensity and an increase in the 533.5 eV peak intensity.

Quantitative analysis of the PDMS based deposited films in Fig. 7 shows the atomic percentage of Zn decreases from 19.81 % in uncoated ZnO, to 17.05 %, 6.28 %, 2.18 %, 2.00 %, 1.03 %, and 0.00 % with 10+ nm of SiO$_2$. Corresponding Si 2p signals are 0.00 %, 13.12 %, 21.24 %, 25.92 %, 27.75 %, 31.96 %, and 38.65 %. The Zn and Si 2p atomic percentages are approximately equal for 11 and 16 nm of SiO$_2$.

We have also performed XPS measurements on PDMS deposited SiO$_2$ films on nanostructured (i.e. non-planar) ZnO NR substrates. These data are shown in the ESI (Fig. S.5), demonstrating even, conformal and completely pinhole-free coverage of such nanostructured substrates. Specifically we have coated ZnO NR arrays with varying aspect ratios (0.5 and 25), to create our core-shell structures. The PDMS based deposition method also allows multiple depositions using smaller masses to be performed to accumulate the same thickness as a single deposition of the equivalent cumulative mass, allowing the precise determination of required mass for a given thickness.

A comparison of Zn 2p intensity of flat ZnO layers coated in one, two and three cycles of 6 mg PDMS-based depositions, with samples coated with either one cycle of 12 or 18 mg PDMS is shown in Fig. 8a, showing excellent agreement in relative intensities, with only slightly increased coating efficiency with multiple smaller depositions, indicating that the SiO$_2$ vapour does not show significant preferential deposition on SiO$_2$

substrates. The Zn 2p peak is shown because it has a much higher relative sensitivity factor than Si 2p, and O 1s (28.72 versus 0.817 and 2.93, respectively, used in CasaXPS), allowing us to better visualise small changes in the coating thicknesses [29]. The same depositions were performed on bare silicon wafers and the thicknesses were measured using SE. The SE data in Fig. 8b shows that n deposition cycles of a given mass x will return a final thickness equal to n times x (n.x) to a high degree of accuracy. The result is quite important as it may allow flat SiO$_2$ film thicknesses greater than 18 nm to be achieved without creating dendritic structures (which begin to be observed when using PDMS source material masses greater than ∼ 65 mg).

We also coated a silicon substrate in two cycles of PDMS-based SiO$_2$ using 40.1 mg of PDMS with the aim of achieving a 20.5 nm deposition (based on the equivalent total PDMS mass used), as shown in Fig. 8(C) and (d). The lack of features in Fig. 8(D) indicates a flat 2D film deposition. The SE fit determined a thickness of 21.4 nm. Cross -sectional SEM shows the film is less uniform than the < 18 nm coatings of Fig. 5. However, the film is more uniform than the single 70.0 mg deposition (1°C/min images of Fig. 2) despite the equivalent mass of this deposition being 80.2 mg. These larger structures may be a consequence of the glancing incidence angle between the PDMS-generated vapour and the substrate, which is known to significantly affect deposit morphology in GLAD techniques [23,25]. A combination of surface trapping and shadowing effects could give rise to these uneven deposits once a
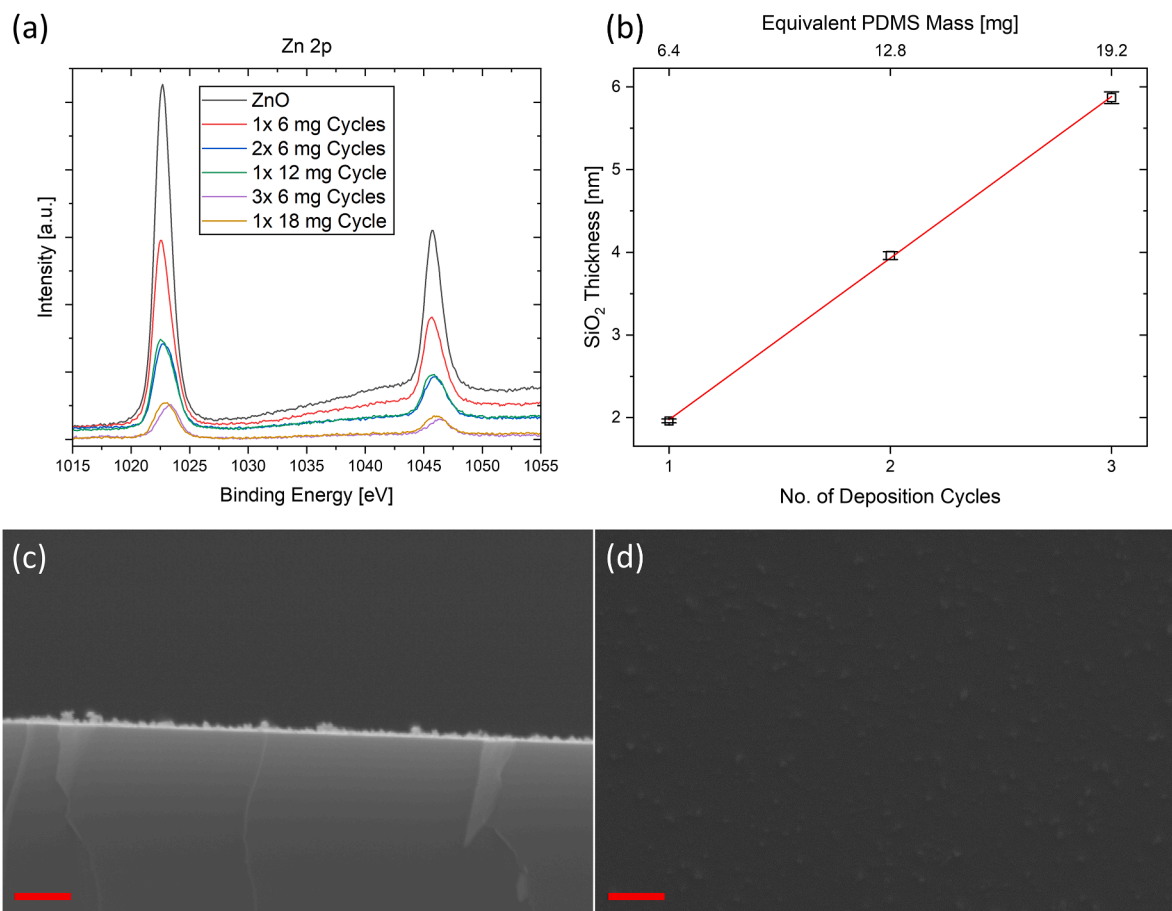
(a)

(b)

(c)

(d)

Fig. 8. Comparison of multiple cycles of PDMS-based SiO$_2$ deposition and single cycles of equivalent total mass showing (a) XPS data for deposition on planar ZnO and (b) SE data for deposition on bare silicon substrates, where the straight red line is the best fit line (c) cross-sectional SEM and (d) top-down SEM images of an SiO$_2$ film deposited by two consecutive deposition cycles of 40.1 mg of PDMS each. The scale bars in (c) and (d) represent 1 μm.

significant amount of vapour is generated from larger PDMS source masses. Further investigation of the effects of deposition angle on morphology will be undertaken in the future. We show some additional results on this topic using ZnO NR arrays in the ESI (Fig. S.6).

As mentioned in section 1.3, the core-shell structure using conductive oxide cores such as ZnO may enable additional device functionality and selectivity by the use of voltages applied to the network of core nanostructures. We have therefore tested the electric breakdown characteristics of our PDMS deposited films, and compared them to high-quality thermal oxide films of the same thickness. These data were analysed using a 2-parameter Weibull distribution [19,20], The data and fits to the linear regions of the datasets are shown in Fig. 9 for the PDMS deposited films and high-quality thermal oxide films. The film thicknesses are 11.5 nm ± 0.5 nm in both cases, enabling meaningful comparison of the films' electrical stability.

The breakdown strengths of the PDMS deposited SiO$_2$ and the industrial thermal oxide can be found from the slopes and intercepts of the linear portion of the data in Fig. 9 using the two parameter Weibull distribution which has the following formula for the cumulative probability of failure (i.e. the fraction of failed devices), F:

$$F = 1 - e^{-\left(\frac{E_b}{\eta}\right)^{\beta}} \quad (2)$$

There are two fit parameters, η and β. The slope of the fit line (when plotted in the linearised form in Fig. 9) equals β and the intercept equals $-\beta\ln(\eta)$. The quantity η represents the scale parameter or 63 % value, i.e. the breakdown field (E_b) when ~ 63 % of the sample set have undergone dielectric breakdown, and is a measure of the breakdown field for the
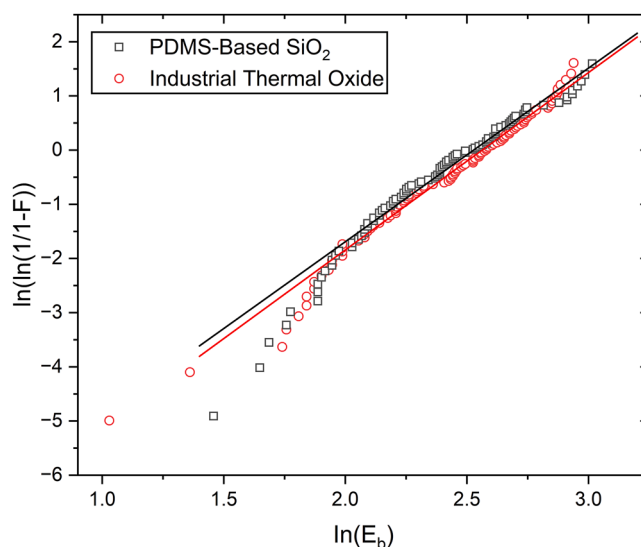

Fig. 9. Weibull distribution plots of breakdown field comparing different 11.5 nm SiO$_2$ films. F indicates the cumulative probability of failure and E_b indicates the breakdown field (in MV/cm). The best fit lines are indicated by solid lines of the appropriate colour in the linear fitted regions of the two data sets. The r^2 values are 0.982 and 0.991, for the PDMS and thermal oxide films, respectively.

Table 1

Fit parameters from Weibull distribution plots comparing different 11.5 nm SiO_2 films.

	PDMS	Thermal oxide
Slope, β	3.21 ± 0.05	3.27 ± 0.03
Intercept, $-\beta\ln(\eta)$	-7.65 ± 0.11	-7.93 ± 0.08
η (MV/cm)	10.89 ± 0.05	11.28 ± 0.03

films. β represents the shape parameter or Weibull slope. The slope and intercept values of the linear fits are in Table 1:

Based on the fits, the values of η for the PDMS and thermal oxide films were found to be 10.84 ± 0.05 MV/cm and 11.30 ± 0.03 MV/cm, respectively. These values are quite close to each other, and are also very close to the expected breakdown field of SiO_2 of ~ 10 MV/cm [30]. The PDMS-based film displays similar leakage current to the thermal oxide at electric fields of 6.5 MV/cm and lower. Above this field strength, the leakage current steadily increases to a single order of magnitude greater at ~ 11.5 MV/cm, at which point breakdown occurs, as shown in Fig. 10. This leakage current is lower than values from the literature for SiO_2 as-deposited by atomic layer deposition (ALD) and comparable to annealed ALD samples, and is much lower than SiO_2 films grown by CVD methods (as-deposited and post anneal) [31,32].

These measurements confirm that the breakdown strength of the PDMS films is comparable to that of high-quality industrial thermal oxides and that these ~ 11.5 nm thick films can sustain applied voltages of the order of 10 V at least as well as the industrial thermal oxide films. Hence the core-shell structure using conductive oxide cores such as ZnO could utilise voltages of this magnitude applied to the network of core nanostructures to enable additional device functionality such as selective attraction or replusion of charged species in solution in a biosensor device, with this functionality further boosted by virtue of local field enhancement effects due to the high aspect ratio nanostructures [33,34].

3.3. DNA Capture Capabilities

Fig. 11 shows the DNA capture efficiency of the SiO_2 nanodendrites, the ZnO-SiO_2 NRs, and uncoated silicon substrates under three different DNA concentrations. We see notable binding to silicon substrates without any nanostructure growth at the lower concentrations. This occurs due to the native oxide of the silicon wafer which is essentially a flat layer of SiO_2 that therefore has an affinity for DNA binding. However, significantly increased DNA capture is achieved by both SiO_2 dendrites and SiO_2 coated ZnO NRs at the larger DNA concentrations, with a much larger capture efficiency achieved by the dendrites at a concentration of 1000 ng/mL of DNA. Despite the decreased capture
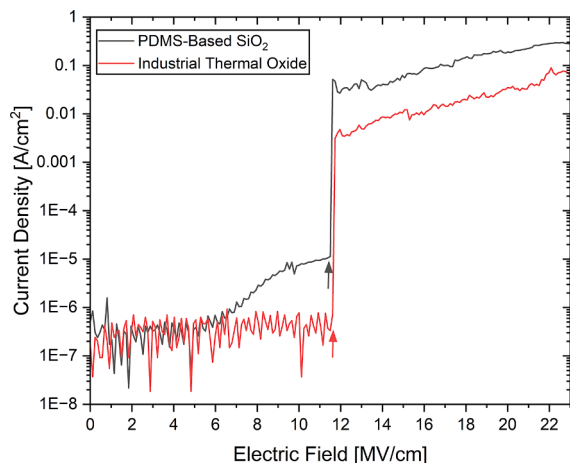
Fig. 10. Current density vs electric field strength for various SiO_2 thin films. The arrows indicate the position of the breakdown field for each sample.
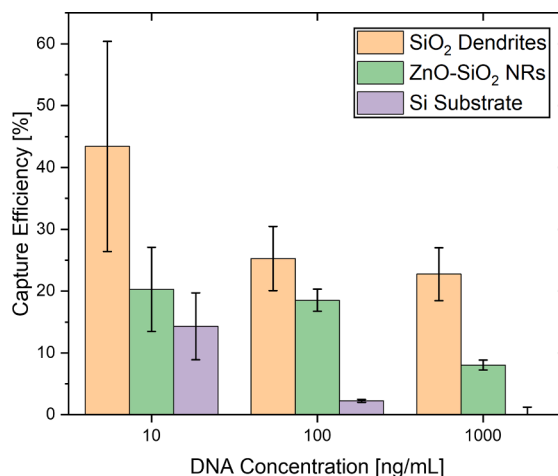
Fig. 11. DNA capture efficiency of three different SiO_2 surface morphologies under various concentrations of DNA within microfluidic chips. The error bars represent the standard deviation of five independent measurements.

efficiencies of the nanostructures with increasing input concentrations of DNA, these values correspond with large amounts of DNA, with the dendrites and NRs capturing 227.3 ± 42.7 ng and 80.4 ± 8.0 ng of DNA respectively from 1000 ng. These quantities far exceed the typical thresholds required for the detection of DNA using quantitative polymerase chain reaction (PCR) to diagnose disease [35].

The increased binding efficiency of the dendrites compared to the SiO_2 coated ZnO NRs is a topic of ongoing study. Our initial hypothesis is that it is possibly related to the combination of high surface to volume ratio and the presence of quite large void regions in the nanodendrite structures, which enable DNA ingress and subsequent capture, compared to the closer packed structure of the SiO_2 coated ZnO NRs. Both nanostructures have similar height (6000 nm), but the NRs are much more tightly packed with an interrod spacing of 200–500 nm compared to the 2000–4000 nm dimension of the voids of the nanodendrite structures. The DNA strands utilised in this study were ~ 3400 nm long (10,000 base pairs) which is much larger than the SiO_2 coated ZnO NR interrod spacing, but comparable to the voids of the nanodendrite structures. The capture efficiency of the NRs might be increased with a decrease in the channel height of the microfluidic chip from 86 μm to a height similar to that of the NRs which could force the solution through the NR array. Despite this, both nanostructure morphologies (SiO_2 nanodendrites and ZnO-SiO_2 NRs) are capable of capturing significant quantities of DNA compared to planar Si surfaces under a variety of conditions and using low cost synthesis and device fabrication technologies. In the future we hope to incorporate these structures into an optimised device design which will maximise their biomolecular capture capabilities.

4. Conclusions

We have demonstrated a novel and straightforward method for deposition of high-quality, nanoscale SiO_2 films and 3D SiO_2 structures using thermal decomposition of polydimethylsiloxane (PDMS), in a furnace in atmospheric pressure at 500 °C. The temperature ramp rate is a key factor in determining the SiO_2 deposit morphology, with slower ramp rates leading to highly conformal 2D films and faster ones yielding 3D nanodentrite structures.

Detailed characterisation using SE, SEM, STEM, FESEM and XPS confirm that this method allows individual nanometre controllability of conformal pinhole-free layers on a variety of materials. For the 2D films the film thickness, as determined by spectroscopic ellipsometry and confirmed by SEM data, is shown to correlate excellently with initial PDMS source material mass in the thickness range 0.8–18 nm.

Depositions on high aspect ratio ZnO nanostructures are shown to be highly conformal, leading to core-shell ZnO-SiO$_2$ nanostructures whose shell thickness is in excellent agreement with the expected values from deposition on planar substrates.

At faster temperature ramp rates an abrupt morphological transition is seen to a deposit which displays a 3D nanodentrite morphology with a high surface to volume ratio.

Electrical breakdown measurements confirm that the breakdown strength of the films is comparable to that of high-quality industrial thermal oxides.

DNA capture measurements confirm both pure SiO$_2$ nanodentrites and ZnO-SiO$_2$ nanostructures are capable of capturing significant quanitities of DNA from low initial concentrations with relatively high efficiency.

Based on these data the SiO$_2$ films and dendritic nanostructures obtained offer significant promise for applications in biosensing and related areas due the relative biocompatibility and affinity of SiO$_2$ for DNA and protein interactions compared to other commonly used materials like gold and silver. The ease of implementation of this method for SiO$_2$ nanoscale deposition means that it can be used in conjunction with other bottom-up nanostructured oxides such as ZnO, which allows the creation of high surface to volume ratio core-shell nanostructures with SiO$_2$ outer shells whose surface properties are well suited to interactions with biological species, as well as directly enabling deposition of a bottom-up 3D nanodentrite structure with an intrinsically high surface to volume ratio.

CRediT authorship contribution statement

Paul Cannon: Writing – original draft, Visualization, Validation, Methodology, Investigation, Funding acquisition, Formal analysis, Data curation. **Enda McGlynn:** Writing – original draft, Supervision, Resources, Methodology, Funding acquisition, Conceptualization. **Darragh O'Neill:** Investigation. **Conor Darcy:** Investigation, Formal analysis. **Erin Rouse:** Investigation. **Robert O'Connor:** Writing – review & editing, Resources. **Brian Freeland:** Writing – review & editing, Supervision. **Barry O'Connell:** Investigation, Formal analysis. **Jennifer Gaughran:** Writing – review & editing, Supervision, Resources, Methodology, Funding acquisition, Conceptualization.

Declaration of competing interest

The authors declare that they have no known competing financial interests or personal relationships that could have appeared to influence the work reported in this paper.

Data availability

Data will be made available on request.

Acknowledgements

Supplementary materials

Supplementary material associated with this article can be found, in the online version, at doi:10.1016/j.apmt.2024.102175.

References

[1] M.A. Dineva, L. Mahilum-Tapay, H. Lee, Sample preparation: a challenge in the development of point-of-care nucleic acid-based assays for resource-limited settings, Analyst 132 (12) (2007) 1193–1199.

[2] R. Boom, C.J.A. Sol, M.M.M. Salimans, C.L. Jansen, P.M.E. Wertheim-Van Dillen, J. Van Der Noordaa, Rapid and simple method for purification of nucleic acids, J. Clin. Microbiol. 28 (3) (1990) 495–503.

[3] N.C. Cady, S. Stelick, C.A. Batt, Nucleic acid purification using microfabricated silicon structures, Biosens. Bioelectron. 19 (1) (2003) 59–66.

[4] L.A. Christel, K. Petersen, W. McMillan, M.A. Northrup, Rapid, automated nucleic acid probe assays using silicon microstructures for nucleic acid concentration, J. Biomech. Eng. 121 (1) (1999) 22–27.

[5] B. Majeed, L. Zhang, N. Tutunjyan, B. Jones, P. Fiorini, D.S. Tezcan, Silicon micro-pillar filter fabrication for DNA separation in Lab-on-chip system, in: Proceedings of the 2012 IEEE 14th Electronics Packaging Technology Conference EPTC 2012, 2012, pp. 52–56.

[6] G. Shtenberg, et al., Picking up the pieces: A generic porous Si biosensor for probing the proteolytic products of enzymes, Anal. Chem. 85 (3) (2013) 1951–1956.

[7] P. Formentín, et al., Effects of SiO2 micropillar arrays on endothelial cells' morphology, N. Biotechnol. 33 (6) (2016) 781–789.

[8] M. Alba, P. Formentín, J. Ferré-Borrull, J. Pallarès, L.F. Marsal, pH-responsive drug delivery system based on hollow silicon dioxide micropillars coated with polyelectrolyte multilayers, Nanoscale Res. Lett. 9 (1) (2014) 1–8.

[9] A. Kabalan, Controlling the doping depth in silicon micropillars, Appl. Sci. 2020 10 (13) (2020) 4581.

[10] J.S. Kim, G.N. Parsons, Nanopatterned area-selective vapor deposition of PEDOT on SiO2vs Si-H: improved selectivity using chemical vapor deposition vs molecular layer deposition, Chem. Mater. 33 (23) (2021) 9221–9230.

[11] K.M.A. Sobahan, Y.J. Park, J.J. Kim, C.K. Hwangbo, Nanostructured porous SiO2 films for antireflection coatings, Opt. Commun. 284 (3) (2011) 873–876.

[12] A. Tereshchenko, et al., Optical biosensors based on ZnO nanostructures: advantages and perspectives. A review, Sens. Actuat. B 229 (2016) 664–677.

[13] M.J. Limo, et al., Interactions between metal oxides and biomolecules: from fundamental understanding to applications, Chem. Rev. 118 (22) (2018) 11118–11193.

[14] L. Ma, B. Liu, P.J.J. Huang, X. Zhang, J. Liu, DNA adsorption by ZnO nanoparticles near its solubility limit: implications for DNA fluorescence quenching and DNAzyme activity assays, Langmuir 32 (22) (2016) 5672–5680.

[15] B. Shi, Y.K. Shin, A.A. Hassanali, S.J. Singer, DNA binding to the silica surface, J. Phys. Chem. B 119 (34) (2015) 11030–11040.

[16] D. Byrne, E. McGlynn, M.O. Henry, K. Kumar, G. Hughes, A novel, substrate independent three-step process for the growth of uniform ZnO nanorod arrays, Thin Solid Films 518 (16) (2010) 4489–4492.

[17] D. Byrne, E. McGlynn, J. Cullen, M.O. Henry, A catalyst-free and facile route to periodically ordered and c-axis aligned ZnO nanorod arrays on diverse substrates, Nanoscale 3 (4) (2011) 1675–1682.

[18] P. Cannon, E. McGlynn, B. Freeland, J. Gaughran, Development and optimisation of a SiO2 PVD technique based on the thermal decomposition of PDMS, New J. Chem. 47 (8) (2023) 3734–3744.

[19] M. Snelgrove, Characterising Infiltration Techniques in Polymer Area Selective Deposition, Dublin City University, 2022.

[20] M. Snelgrove, et al., Growth chemistry and electrical performance of ultrathin alumina formed by area selective vapor phase infiltration, Microelectron. Eng. 266 (2022) 111888.

[21] C. Camino, S.M. Lomakin, M. Lazzari, Polydimethylsiloxane thermal degradation Part 1. Kinetic aspects, Polymer 42 (6) (2001) 2395–2402.

[22] G. Camino, S.M. Lomakin, M. Lageard, Thermal polydimethylsiloxane degradation. Part 2. The degradation mechanisms, Polymer 43 (7) (2002) 2011–2015.

[23] M.T. Taschuk, M.M. Hawkeye, M.J. Brett, Glancing angle deposition. Handbook of Deposition Technologies for Films and Coatings: Science, Applications and Technology, 2010, pp. 621–678.

[24] A. Garcia-Valenzuela, R. Alvarez, V. Rico, J. Cotrino, A.R. Gonzalez-Elipe, A. Palmero, Growth of nanocolumnar porous TiO2 thin films by magnetron sputtering using particle collimators, Surf. Coat. Technol. 343 (2018) 172–177.

[25] C. Lopez-Santos, et al., Nanocolumnar association and domain formation in porous thin films grown by evaporation at oblique angles, Nanotechnology 27 (39) (2016) 395702.

[26] M.P. Seah, W.A. Dench, Quantitative electron spectroscopy of surfaces: A standard data base for electron inelastic mean free paths in solids, Surf. Interface Anal. 1 (1) (1979) 2–11.

[27] NIST Standard Reference Database 71 | NIST. https://www.nist.gov/srd/nist-standard-reference-database-71.

[28] F.A. Stevie, C.L. Donley, Introduction to x-ray photoelectron spectroscopy, J. Vac. Sci. Technol. A 38 (6) (2020).

[29] N. Fairley, et al., Systematic and collaborative approach to problem solving using X-ray photoelectron spectroscopy, Appl. Surf. Sci. Adv. 5 (2021) 100112.

[30] B. El-Kareh, Thermal oxidation and nitridation, Fundam. Semicond. Process. Technol. (1995) 39–85.

[31] G.H. Baek, et al., Atomic layer chemical vapor deposition of SiO$_2$ thin films using a chlorine-free silicon precursor for 3D NAND applications, Ceram. Int. 47 (13) (2021) 19036–19042.

[32] M. Sometani, R. Hasunuma, M. Ogino, H. Kuribayashi, Y. Sugahara, K. Yamabe, Suppression of leakage current of deposited SiO$_2$ with bandgap increasing by high temperature annealing, ECS Trans. 19 (2) (2009) 403–413.

[33] S. Garry, É. McCarthy, J.P. Mosnier, E. McGlynn, Influence of ZnO nanowire array morphology on field emission characteristics, Nanotechnology 25 (13) (2014) 135604.

[34] R.T. Rajendra Kumar, et al., Control of ZnO nanorod array density by Zn supersaturation variation and effects on fieldemission, Nanotechnology 18 (21) (2007) 215704.

[35] A. Szpechcinski, M. Dancewicz, P. Kopinski, J. Kowalewski, J. Chorostowska-Wynimko, Real-time PCR quantification of plasma DNA in non-small cell lung cancer patients and healthy controls, Eur. J. Med. Res. 14 (SUPPL.4) (2009) 237–240.